In-situ growth of nanowire $WO_{2.72}$ on carbon cloth as a binder-free electrode for flexible asymmetric supercapacitors with high performance

Xiao Huang[a], Zhiguo Zhang[a] ,Huan Li[a], Hongxia Wang[b], Tingli Ma[a,c*]

[a] *Department of Life Science and System Engineering, Kyushu Institute of Technology, Kitakyushu 8080134, Japan.*

[b] *School of Chemistry, Physics and Mechanical Engineering, Queensland University of Technology Brisbane QLD4001, Australia*

[c] *School of Petroleum and Chemical Engineering, Dalian University of Technology, Dalian 124221, Liaoning China.*

[*] Corresponding author. Email: tinglima@life.kyutech.ac.jp (T. Ma).

Abstract

For the first time, $WO_{2.72}$ nanowires were in-situ grown on carbon cloth by a simple solvothermal reaction. The nanowire $WO_{2.72}$/carbon cloth (NW $WO_{2.72}$/CC) electrode showed good electrochemical performance with specific capacitance (Cs) reaching up to 398 F g^{-1} at a current density of 2 A g^{-1}. The capacitance of 240 F g^{-1} was retained at a high current density of 16 A g^{-1}. To further evaluate the energy storage performance, flexible asymmetric supercapacitors (FASCs) were fabricated using the activated carbon/carbon cloth (AC/CC) as negative electrode and NW $WO_{2.72}$/CC as positive electrode, respectively. The FASCs delivered a high energy density of 28 Wh kg^{-1} at a power density of 745 W kg^{-1} and 13 Wh kg^{-1} even at a high power density of 22.5 kW kg^{-1}. More impressively, 81% of the specific capacitance of the FASCs was retained after 10000 cycles, indicating excellent cycle stability. This work indicates the NW $WO_{2.72}$/CC holds a great potential for application in energy storage devices.

Keywords: solvothermal reaction; asymmetric supercapacitors; high energy density; flexibility;

1. Introduction

Supercapacitors (SCs), also known as electrochemical capacitors or ultra-capacitors, have drawn great attention as an important energy storage device with high power density, long cycle life and safety [1-2]. Electrochemical capacitors include electrochemical double-layer capacitors (EDLCs) and pseudo-capacitors[3]. The former stores charge via ion adsorption while the latter

operates through reversible Faraday redox reactions occurring at the electrode/ electrolyte interfaces, as well as in the bulk near the surface of the electrode [4-6]. Generally, pseudo-capacitors show higher energy density compared to EDLCs because of the additional charges transferred within the defined potential as a result of Faradaic reactions. However, the energy density of SCs is still much lower than that of batteries, which hinders their practical applications in areas which requires both high energy density and high power density [7]. According to the equation of $E=1/2CV^2$, the energy density can be improved by enhancing Cs and the operating voltage window of the device[8]. Typically, the operating voltage for symmetric supercapacitors (SSCs) using aqueous electrolyte is less than 1.0 V because water molecule will break down above 1.0 V. Nevertheless, the operation voltage can be increased to 1.0~2.0 V through using asymmetric supercapacitor (ASCs) architecture by taking advantages of different potential of the two electrodes in ASCs. Meanwhile Cs of SCs can be enhanced by increasing conductivity and active site of electrode material [7,-9]. Transition metal oxides (TMOs) which have variable valence state for redox reactions such as RuO_2, WO_{3-x}, NiO_x, CoO_x, MnO_x, FeO_x, etc have demonstrated high specific capacitances (Cs) compared to carbon based materials [10-16]. However, the intrinsically poor electrical conductivity leads to low rate-capability and poor cycle life, which hinders their practical application in supercapacitors [17-21]. To overcome this issue, development of materials with better conductivity is urgently needed.

Tungsten oxides (WO_x, $2<x<3$), as an important member of TMOs, have been drawing great attention, which have various oxidation [11]. They exhibited distinctive physical and chemical properties due to their abundant surface oxygen vacancies (SOVs) [22-23]. Among the various WO_x, $WO_{2.72}$ attracted most interest because of its largest content of SOVs. Moreover, it is the most stable form and possess good conductivity making it a promising candidates for

various application such as photocatalysts, electrochromic devices, field-emitting devices and gas sensors [24-27]. Nevertheless, up to now, there are limited reports about application of $WO_{2.72}$ in supercapacitor. Sangbaek Park et al reported that 3-D urchin-like $WO_{2.72}$ nanostructure electrodes demonstrated specific capacitance of 309 F g^{-1} at 2 A g^{-1} in traditional three electrode [28]. Moreover, Zhao et al showed that the specific capacitance of $WO_{2.72}$ on FTO-coated glass was 440 F g^{-1} at 2A g^{-1} when the electrode was tested in three electrode cell system using 1M H_2SO_4 aqueous electrolyte solution which had an electrochemical window of −0.5 to 0 V [25]. Obviously, the specific capacitance of FTO substrate based $WO_{2.72}$ was much higher. Hence, the electrode prepared by in-situ method is more beneficial to the electrochemical performance improvements. Up to now, NW $WO_{2.72}$ based FASCs have not been reported.

Herein, we report a supercapacitor electrode based on NW $WO_{2.72}$ /CC. The NW $WO_{2.72}$/CC was prepared by a facile in-situ solvothermal method. The $WO_{2.72}$ nanowires formed intercrossed network structure, which provided more active sites and shortened the ion diffusion length. The NW $WO_{2.72}$/CC had well chemical stability and structure stability. The NW $WO_{2.72}$/CC electrode exhibited a high Cs of 398 F g^{-1} (1433 mAh g^{-1}) at a current density of 2 A g^{-1} with their unique morphology and structure stability. Furthermore, flexible asymmetric supercapacitors (FASCs) with structure of NW $WO_{2.72}$/CC //Poly (vinyl alcohol) (PVA/LiCl gel//AC/CC demonstrated high energy density of 28 Wh kg^{-1} at a power density of 745 W kg^{-1}, which makes it a prospective candidate for energy storage devices.

2. Experimental section

2.1 Preparation of NW $WO_{2.72}$/CC

Prior to the synthesis of NW $WO_{2.72}$/CC, CC was pre-treated by nitric acid at 120 °C for 2 h and then thoroughly washed with deionized water several times and dried under vacuum

overnight. For the preparation of NW $WO_{2.72}$/CC, firstly, CC was put into autoclave containing 0.05 g of WCl_6 dissolved in 50 mL absolute ethanol. The autoclave was heated to 180 ℃ and remained at the temperature for 24 h. After cooling to room temperature, the samples were washed by ethanol and then dried at 50 ℃ under vacuum for 10 h. The mass loading of the NW $WO_{2.72}$ was about 2 mg cm^{-2}.

2.2 Preparation of polymer gel electrolyte

Gel polymer electrolyte was prepared via solution casting method by modifying the procedure reported in previous work [29]. Firstly, 4 g of PVA was dissolved in 40 mL deionized water and stirred until the solution became clear. Then a solution containing 8.5 g LiCl in 10 ml deionized water was slowly added into the PVA solution under magnetic stirring. Finally, the sticky solution was transferred to PET (Polyethylene terephthalate) dish. After dried at room temperature for about 24 h~72 h, PVA/LiCl gel was obtained.

2.3 Preparation of activated carbon electrode and fabrication of flexible asymmetric supercapacitors

The negative electrode of AC/CC was prepared by spraying method. Firstly, a slurry containing 80wt. % activated carbon, 10wt. % acetylene black as conductive material additives and 10wt. % polytetrafluoroethylene (PTFE) as binder dispersed in ethanol was prepared. After sonication for 30 min, the mixture was sprayed onto a pre-treated carbon cloth and then dried under vacuum overnight. Flexible asymmetric supercapacitors with sandwich structure of NW $WO_{2.72}$/CC positive electrode PVA-LiCl gel electrolyte /AC/CC negative electrode were assembled based on the charge balance theory:

$$\frac{m_+}{m_-} = \frac{C_- \times \Delta V_-}{C_+ \times \Delta V_+}$$

Therefore, the optimal ratio between the positive electrode and negative electrode was 1/1.8 in the flexible solid state ASCs.

2.4 Characterization of materials

The crystal structure of the as-synthesized material was characterized by powder X-ray diffraction (XRD; RIGAKU, model D/max-2500 system at 40 kV and 100 mA of Cu Ka). The composition of the product was identified by Fourier transform infrared (FTIR) spectrum. The morphologies were observed by a Field emission scanning electron microscope (FESEM; HITACHI, S-5200, Japan). The microstructures of the samples were examined by transmission electron microscopy (TEM, Tecnai F30) operated at 300 kV. The X-ray photoelectron spectroscopy (XPS) spectra were carried on a PHI 5000 Versa Probe II (ULVAC−PHI, Inc, Japan) system with monochromatic Al-Ka source (h=1486.6 eV).

2.5 Electrochemical measurements

All the electrochemical performance were carried out on Solartron 1287 Potentiostat Galvanostat and 1255B Frequency Response Analyzer electrochemical workstation. The electrochemical behaviors of the NW $WO_{2.72}$/CC (1×1 cm^2) firstly were tested in a traditional three electrode cell system. Ag/AgCl (KCl, saturated) electrode and platinum gauze were used as reference electrode and counter electrode, respectively. Measurements of cyclic voltammetry (CV) at various scanning rates and galvanostatic charge/discharge (GCD) at different current densities were performed. The electrochemical impedance spectra (EIS) were evaluated in the frequency range of 10^{-2} ~10^6 Hz with 10 mV amplitude at open circuit potential. The specific capacitance was determined from the discharge curves according to the following equation:

$$Cs=\frac{I\Delta t}{m\Delta v} \quad (1)$$

Where Cs, I, Δt, m and Δv are the specific capacitance (F g^{-1}), discharge current (A), discharge time (s), active material (g) and electrochemical window, respectively.

The energy density and power density of the flexible asymmetric supercapacitors were also calculated based on the following equations, respectively.

$$E=\frac{C\times V^2}{2} \quad (2)$$

$$P=\frac{E}{\Delta t} \quad (3)$$

Where E, C, V and P are the energy density (Wh kg^{-1}), specific capacitance, operating voltage, and power density (P, W kg^{-1}), respectively.

3. Results and discussion

3.1 Materials characterization

Fig. 1

Fig. 1 illustrates the fabrication processes of NW $WO_{2.72}$/CC. Firstly, CC was pre-treated in nitric acid to increase the active sites of carbon cloth for growth of $WO_{2.72}$. The NW $WO_{2.72}$ was in-situ grown on the surface of CC by a simple solvothermal reaction. For comparison, NW $WO_{2.72}$ powder was also prepared.

Fig. 2

The morphologies of bare CC and the obtained solvothermal products were characterized by FESEM. As shown in Fig. 2a, CC consists of fibres with smooth surface. After treatment with nitric acid, the surface of the fibres becomes rough (Fig. 2b and 2c), which promotes the growth of NW $WO_{2.72}$. After solvothermal reaction, the surface of CC is uniformly covered by the nanowires (Fig. 2d). Moreover, the nanowires are interweaved to form a network, which creates porous structure for transport of electrolyte ion during the charge/discharge electrochemical process (Fig. 2e and 2f) [25].

Fig. 3

TEM was used to get further insights into the microstructure of the obtained NW $WO_{2.72}$/CC. As shown in Fig. 3a, the nanowires inter-cross together creating amount of porous structure, which is beneficial to the ion diffusion and contact with electrolyte. Furthermore, the TEM image at high resolution (Fig. 3c) confirms that the diameter of the nanowires is about 20 nm and the interplanar spacing is 0.38 nm [28]. More importantly, it is observed that the nanowires preferentially grow along the [010] direction [24,-28].

Fig. 4

The XRD was used to identify the material phase and crystal structure of the synthesized sample. $WO_{2.72}$ is a monoclinic structure (a =18.32, b =3.79, and c =14.04 Å), which is strongly anisotropic and incorporates an ordered 2-D lattice. The corner sharing of 2-D lattice is distorted and WO_6 octahedra is tilted which are connected in a, b and c direction, thereby forming a three-dimensional structure (inset in Fig. 4) [24,-28]. The two obvious peaks located at 23.5° and 47.9° are the characteristic peaks of $WO_{2.72}$ (JCPDS file #65-1291), which are indexed to the (010) and (020) planes, respectively. The strongest peak of (010) suggests the preferential crystal growth direction, which is consistent with the previous TEM results analysis. The broad peaks located at 26.1° and 43.5° are attributed to the CC [25]. Furthermore, Fourier transform infrared (FTIR) spectrum suggests the surface of our sample is clean with no organic residual detected in the spectrum (Fig. S4 in the Supporting Information) [24].

Fig. 5

XPS was utilized to investigate the chemical composition and surface chemical states. The corresponding results are shown in Fig. 5. The full range of spectra confirms the existence of W, O, and C elements. The spectrum of O1s displays a wide and obvious asymmetric peak. The main peak is located at 530.5 V, attributed to the O bond in $WO_{2.72}$. The weak peak located at

higher binding energy of 532.2 V may result from C-O bond/H-O bond [22]. While for the spectra of W4f (given in Fig. 5c), the main peaks of W4$f_{5/2}$ and W 4$f_{7/2}$ located at 37.8 eV and 35.7 eV, respectively, are attributed to the 6+ valence state of W atoms. Additionally, the lower binding energy at 34.6 and 37.1 eV are due to the emission of W 4$f_{5/2}$ and W 4$f_{7/2}$ from the W atoms in an oxidation state of 5+ [22]. The XPS fitting results clearly demonstrated that the W5+/W6+ ratio of W−OV−W is (0.92 ± 0.03). These results have been reported previously. Compared to stoichiometry, the XPS spectra confirm that there are abundant oxygen vacancies in $WO_{2.72}$. More oxygen vacancies give rise to better conductivity which is conducive to the electrochemical performance.

3.2 Electrochemical properties of NW $WO_{2.72}$/CC electrodes

Fig. 6

The electrochemical properties of NW $WO_{2.72}$/CC electrodes were tested by traditional three-electrode configuration in 5M LiCl aqueous solution. CV curves at various scanning rates within the range of −0.4 to 0.6 V are shown in Fig. 6a. The profiles illustrate that the electrode reveals pseudocapacitive behaviors. The involved redox reaction are owned to the insertion/extraction of electrons and Li^+ ions, described as the following equation:

$$WO_{2.72}+xe^-+xLi^+ \leftrightarrow Li_xWO_{2.72}$$

During the charge process, the electrons from the electrode and the Li^+ ions from the LiCl electrolyte are co-inserted into $WO_{2.72}$ [27,-30]. A reverse process occurs in the discharge process. Traditionally, the faradaic reaction occurs at the electrode/electrolyte interface. In our case, Li ions can insert into $WO_{2.72}$ as well, therefore providing enhanced capacitance apart from the surficial reaction [4]. In addition, the CV curves show that, with the increase of scanning rates, the current densities increases without distortion in the CV curves, indicating good conductivity and reversibility of the electrode material.

Understanding the working mechanism is significantly important. In our work, we investigate the mechanism from the knowledge of charge storage. For our work, the electrode stores charge mainly from two components. The first component (referred to as pseudocapacitance) is the intercalation contribution from the Li^+ ion insertion process and the faradaic contribution from the surface charge-transfer process [30]. The big difference between the intercalation–pseudocapacitive material and battery-type material is that there is phase change for the latter material [30]. The second component is the nonfaradaic contribution that is from the EDLCs. These charge storage mechanism were characterized by analyzing the CV data at various scanning rates according to the following equation:

$$i = av^b$$

The two limit value of b is 0.5 and 1.0. For b=0.5, it suggests the material for electrode is battery-type and the current is proportional to $v^{1/2}$(scanning rate) [31]. While the other limit value of b=1 represents pseudocapacitive (including capacitive) response and the current is proportional to v [31]. Actually, for most materials, b is not a constant value. The data for the NW $WO_{2.72}$/CC electrode are shown in Fig. S6. The b-values are in the range of 0.8−1.0, indicating that the current response is predominantly pseudocapacitive and EDLCs behaviour. This behaviour reaches an agreement with the previous work reported by Yury Gogotsi and Bruce Dunn [30-31].

To determine the specific capacitances, GCD curves were measured at different current densities in a fixed potential window of −0.4~0.6 V. The GCD curves are almost symmetric, indicating excellent reversibility and high Coulombic efficiency. It also indicates the material adopts capacitive behaviour instead of batteries behaviour. The specific capacitance calculated from the discharge curve is 398 F g^{-1} at a current density of 2 A g^{-1}. Moreover, the specific capacitance remains at 240 F g^{-1} even at a much higher current density of 16 A g^{-1}. Obviously, NW $WO_{2.72}$/CC electrodes exhibit higher specific capacitance than previously reported metal oxides on carbon fiber paper or carbon textile cloth as substrates [32-34]. The cycle performance at current density of 6 A g^{-1} was also performed as presented in Fig. 6d. The initial specific capacitance is 325 F g^{-1}. After 3000 cycles, the specific capacitance of the electrode retains 92% of the initial value. The electrochemical performance of activated carbon cloth was also

measured. The results indicate that the contribution of activated carbon cloth is ignorable (shown as in Fig. S7).

Based on the previous results analysis, the NW $WO_{2.72}$/CC electrode showed good electrochemical performance. The reasons can be concluded as the following: (1) $WO_{2.72}$ with amount of oxygen vacancies possess well conductivity intrinsically [25]; (2) carbon cloth show well conductivity and mechanical flexibility [35]; (3) pre-treated by nitric acid leads to rough surface of carbon cloth, which ensure the firm in situ growth of NW $WO_{2.72}$ on carbon cloth, this binder-free and direct growth provides rich and fast charge transport channels between the CC substrate and NW $WO_{2.72}$ [11]; (4) the 3-D network composed of interweaved NW $WO_{2.72}$ can further expose much effective sites for redox reactions and shorten the ion diffusion distance between the electrolyte and electrode [5].

Fig. 7

An electrochemical impedance spectroscopy (EIS) of the NW $WO_{2.72}$/CC electrode was measured under an AC perturbation potential of 10 mV in the frequency range of 10^{-2}~10^{6} Hz to get further understanding of the electrochemical behavior of the NW $WO_{2.72}$/CC electrode in 5M LiCl aqueous solution. As shown in Fig. 7a, the Nyquist plots consist of two distinct parts including a semicircle at high frequency and a straight line at the low frequency range [5]. The semicircle at high frequency is more likely related to the interfacial charge transfer resistance (Rct) while the low frequency feature is related with ions diffusion in the electrolyte with slope around 45° [36]. Fitting the EIS using the equivalent circuit shows Rct is 13.5 Ω. The intercept of the Nyquist plot on the real axis represents series resistance (Rs) which is mainly due to solution resistance. The obtained Rs = 6 Ω indicates the low series resistance of the electrode. Thus the relaxation time constant of τ_0 is 0.3 s calculated by the equation of $\tau_0 = 1/f_0$, suggesting well conductivity and fast ion diffusion [36].

Flexible asymmetric supercapacitors were fabricated using the NW $WO_{2.72}$/CC as positive electrode and activated carbon sprayed on carbon cloth (AC/CC) as negative electrode. The amount of active carbon on AC/CC is determined according to the charge balance theory of both electrodes. The electrochemical performance of AC/CC is shown in Fig. S8. As observed in Fig.

S8, the CV curves of AC/CC are quasi-rectangular shapes, indicating EDLCs behavior. The shape the CV plots are retained with the increase of scanning rates from 2 mV s^{-1} to 100 mV s^{-1}. The GCD curves under different current densities are equicrural triangles, which demonstrates that the capacitance is mainly from EDLC.

Fig. 8

The structure of the FASCs is shown as in Fig. 8a. The operating voltage of the FASCs is increased to 1.5 V, much higher than that of NW $WO_{2.72}$//PVA/H_2SO_4//NW $WO_{2.72}$ SSCs. The broader operating voltage window is favorable for improving the energy density of the system. The electrochemical performance of the FASCs measured by CV and GCD under different current densities and scan rate (from 2 to 100 mV s^{-1}) are given in Fig. 8b. The CV curves show the combination of pseudocapacitive properties of $WO_{2.72}$ and EDLCs features of AC [37]. GCD at different current densities (1~30 A g^{-1}) are employed in order to calculate the specific capacitance of the FASCs. The curves show IR (I= current, R= resistance) drops, which may be due to the internal resistance and inferior electrons collection of CC compared to metal based substrate [11,-35]. The specific capacitance calculated from the discharge curves are illustrated in Fig. 8d. A high specific capacitance of 90 F g^{-1} is acquired at a current density of 1 A g^{-1}. Even when the current density increases to 30 A g^{-1}, the specific capacitance still remains 40 F g^{-1}. The Ragon plot of the FASCs in Fig. 8e shows the relationship of the energy density versus power density. The highest energy density can reach up to 28 Wh kg^{-1} at a power density of 745 W kg^{-1}. When the power density is increased to 22.5 kW kg^{-1}, the energy density still maintains 13 Wh kg^{-1}. This is substantially higher than the performance of other ASCs reported previously such as carbon nanotubes (CNTs)/MnO_2//CNTs/polyaniline (PANI)-ASCs (24.8 Wh kg^{-1} at 120 W kg^{-1}) [38], MnO_2@activated multihole carbon (AMC)//activated graphene (18.04 W h kg^{-1} at 8.97 W kg^{-1}) [39], CNF/MnO_2//CNF/Fe_2O_3 (22.8 W h kg^{-1} at 159.4 W kg^{-1}) [40], CNT@NiO//PCPs (25.4 Wh kg^{-1} at 400 W kg^{-1}) [12], $NiCo_2O_4$//AC (15.42 W h kg^{-1}) [41]. The cycle performance of the FASCs is further investigated by repeated charge/discharge process at a larger current density of 16 A g^{-1}(Fig. 8f). The plot shows that the specific capacitance gradually decreases with cycling number in the first 2000 cycles. After this, the specific capacitance is then slightly increased. Similar phenomenon of specific capacitance recovery was also observed in Li-ion battery (sulfur–carbon composite as working electrode), which is generally ascribed to more

efficient contact between electrolyte and the electrode [42-43]. Importantly, the specific capacitance has no obvious decrease after 7000 cycles. The specific capacitance remains 90% after 5000 cycles and 81% after 10000 cycles, indicating good stability. To prove the mechanical flexibility, the device was twisted and bended. The Fig. S11 showed the device could remain its construction after various bending conditions. More importantly, the electrochemical performance of the device had no significant change under different curvatures.

4. Conclusions

In summary, we use in-situ method to fabricate NW $WO_{2.72}$/CC. The high specific capacitance 398 F g^{-1} is obtained in 3-electrode system. The flexible asymmetric supercapacitors show well electrochemical performance. The specific capacitance is reached up to 90 F g^{-1} at a current density of 1 A g^{-1}. More importantly, the device exhibits high energy density of 28 Wh kg^{-1} at a power density of 745 W kg^{-1} and long cycle stability with 81% capacitance retention after 10000 cycles. Therefore, NW $WO_{2.72}$/CC electrode has a potential for electric energy storage system.

Acknowledgments

This work was supported by the Grant-in-Aid for Scientific Research (KAKENHI) program, Japan (C, Grant Number 15K05597) and Takahashi Industrial and Research center for Solar Light Energy Conversion, Kyushu Institute of Technology.

References

[1] D.P. Dubal, O. Ayyad, V. Ruiz, P. Gomez-Romero, Chem. Soc. Rev. 44 (2015) 1777-1790.
[2] W. Zuo, R. Li, C. Zhou, Y. Li, J. Xia, J. Liu, Adv. Sci. 4 (2017) 1600539-1600559.
[3] Y. Jiang, C. Zhou, J. Liu, Energy Storage Mate. 11 (2018) 75-82.
[4] Y. Wang, Y. Song, Y. Xia, Chem. Soc. Rev. 45 (2016) 5925-5950.
[5] X. Huang, Z. Zhang, H. Li, Y. Zhao, H. Wang, T. Ma, J. Alloys Compd. 722 (2017) 662-668.
[6] Z. Zhang, X. Huang, H. Li, Y. Zhao, T. Ma, Appl. Surf. Sci. 400 (2017) 238-244.
[7] N. Choudhary, C. Li, J. Moore, N. Nagaiah, L. Zhai, Y. Jung, J. Thomas, Adv. Mater. 29 (2017) 1605336-1605365.
[8] W. Zuo, C. Xie, P. Xu, Y. Li, J. Liu, Adv. Mater. 29 (2017) 1703463-1703471.
[9] T. Wang, S. Zhang, X. Yan, M. Lyu, L. Wang, J. Bell, H. Wang, ACS Appl. Mater. & Interfaces 9 (2017) 15510-15524.
[10] R.B. Rakhi, W. Chen, M.N. Hedhili, D. Cha, H.N. Alshareef, ACS Appl. Mater. & Interfaces 6 (2014) 4196-4206.
[11] X. Lu, T. Zhai, X. Zhang, Y. Shen, L. Yuan, B. Hu, L. Gong, J. Chen, Y. Gao, J. Zhou, Y. Tong, Z.L. Wang, Adv. Mater. 24 (2012) 938-944.
[12] H. Yi, H. Wang, Y. Jing, T. Peng, X. Wang, J. Power Sour. 285 (2015) 281-290.

[13] Z. Zhang, Y. He, Q. Zhou, C. Huang, X. Zhang, Z. Guo, Y. Gao, J. Liu, Z. Cao, Electrochim. Acta 144 (2014) 300-306.
[14] M. Huang, Y. Zhang, F. Li, L. Zhang, Z. Wen, Q. Liu, J. Power Sour. 252 (2014) 98-106.
[15] J. Xu, Q. Wang, X. Wang, Q. Xiang, B. Liang, D. Chen, G. Shen, ACS Nano 7 (2013) 5453-5462.
[16] H. Xu, X. Hu, H. Yang, Y. Sun, C. Hu, Y. Huang, Adv. Energy Mater. 5 (2015) 1401882-1401888.
[17] P. Asen, S. Shahrokhian, J. Phy. Chem. C 121 (2017) 6508-6519.
[18] Q. Wang , J. Xu, X. Wang, B. Liu, X. Hou, G. Yu, P. Wang, D. Chen, G. Shen, ChemElectroChem 1 (2014) 559-564.
[19] H. Wang, Z. Xu, H. Yi, H. Wei, Z. Guo, X. Wang, Nano Energy 7 (2014) 86-96.
[20] R. Mondal, S. Sahoo, C.S. Rout, Am. J. Eng. Appl. Sci. (2016).
[21] X. Lu, M. Yu, G. Wang, T. Zhai, S. Xie, Y. Ling, Y. Tong, Y. Li, Adv. Mater. 25 (2013) 267-272.
[22] H. Zhou, Y. Shi, Q. Dong, J. Lin, A. Wang, T. Ma, J. Phy. Chem. C 118 (2014) 20100-20106.
[23] H. Zhou, Y. Shi, Q. Dong, Y. Wang, C. Zhu, L. Wang, N. Wang, Y. Wei, S. Tao, T. Ma, J. Mater. Chem. A 2 (2014) 4347-4354.
[24] G. Xi, S. Ouyang, P. Li, J. Ye, Q. Ma, N. Su, H. Bai, C. Wang, Angew. Chem. Int. Edit. 51 (2012) 2395-2399.
[25] Y. Tian, S. Cong, W. Su, H. Chen, Q. Li, F. Geng, Z. Zhao, Nano Letters 14 (2014) 2150-2156.
[26] D.R. Shinde, P.G. Chavan, S. Sen, D.S. Joag, M.A. More, S.C. Gadkari, S.K. Gupta, ACS Appl. Mater. Interfaces 3 (2011) 4730-4735.
[27] B.J.W. Liu, J. Zheng, J.L. Wang, J. Xu, H.H. Li, S.H. Yu, Nano Letters 13 (2013) 3589-3593.
[28] S. Park, H.W. Shim, C.W. Lee, H.J. Song, J.C. Kim, D.-W. Kim, Nano Research 9 (2016) 633-643.
[29] N. Batisse, E. Raymundo-Piñero, J. Power Sour. 348 (2017) 168-174.
[30] M.R. Lukatskaya, B. Dunn, Y. Gogotsi, Nat. Commun. 7 (2016) 12647-12659.
[31] J. Wang, J. Polleux, J. Lim, B. Dunn, J Phy. Chem. C 111 (2007) 14925-14931.
[32] L. Feng, G. Li, S. Zhang, Y.X. Zhang, Ceram. Int. 43 (2017) 8321-8328.
[33] T. Wang, D. Song, H. Zhao, J. Chen, C. Zhao, L. Chen, W. Chen, J. Zhou, E. Xie, J Power Sour. 274 (2015) 709-717.
[34] M. Yu, T. Zhai, X. Lu, X. Chen, S. Xie, W. Li, C. Liang, W. Zhao, L. Zhang, Y. Tong, J Power Sour. 239 (2013) 64-71.
[35] G. Wang, H. Wang, X. Lu, Y. Ling, M. Yu, T. Zhai, Y. Tong, Y. Li, Adv. Mater. 26 (2014) 2676-2682.
[36] L. Yuan, X.-H. Lu, X. Xiao, T. Zhai, J. Dai, F. Zhang, B. Hu, X. Wang, L. Gong, J. Chen, C. Hu, Y. Tong, J. Zhou, Z.L. Wang, ACS Nano 6 (2012) 656-661.
[37] H. Quan, B. Cheng, D. Chen, X. Su, Y. Xiao, S. Lei, Electrochim. Acta 210 (2016) 557-566.
[38] Y. Jin, H. Chen, M. Chen, N. Liu, Q. Li, ACS Appl. Mater. Interfaces 5 (2013) 3408-3416.
[39] S. Zhu, W. Cen, L. Hao, J. Ma, L. Yu, H. Zheng, Y. Zhang, Mater. Lett. 135 (2014) 11-14.
[40] P. Yang, Y. Ding, Z. Lin, Z. Chen, Y. Li, P. Qiang, M. Ebrahimi, W. Mai, C.P. Wong, Z.L. Wang, Nano Letters 14 (2014) 731-736.
[41] X.F. Lu, D.J. Wu, R.Z. Li, Q. Li, S.H. Ye, Y.X. Tong, G.R. Li, J. Mater.Chem. A 2 (2014) 4706-4713.
[42] X.P. Gao, H.X. Yang, Energy Environ Sci. 3 (2010) 174-189.
[43] C. Lai, X. P. Gao, B. Zhang, T. Y. Yan, Z. Zhou, J. Phy. Chem. C, 113 (2009) 4712-4716.

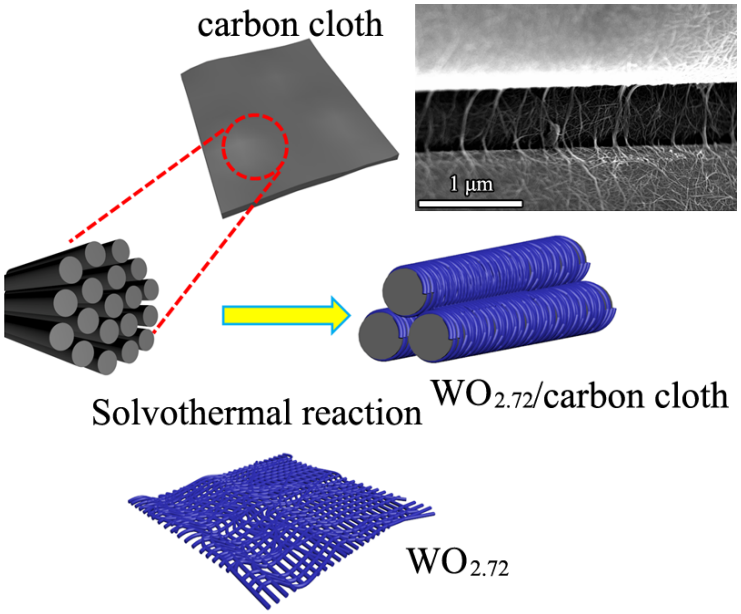

Fig. 1 Process for grown nanowire $WO_{2.72}$/carbon cloth.

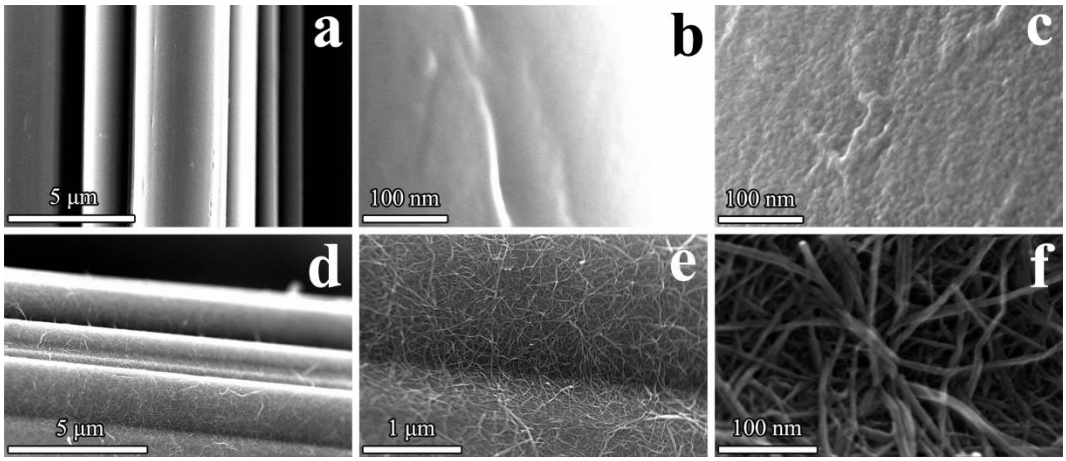

Fig. 2 SEM images of (a, c) carbon cloth pre-treated by nitric acid, (b) carbon cloth, (d–f) nanowire $WO_{2.72}$/carbon cloth.

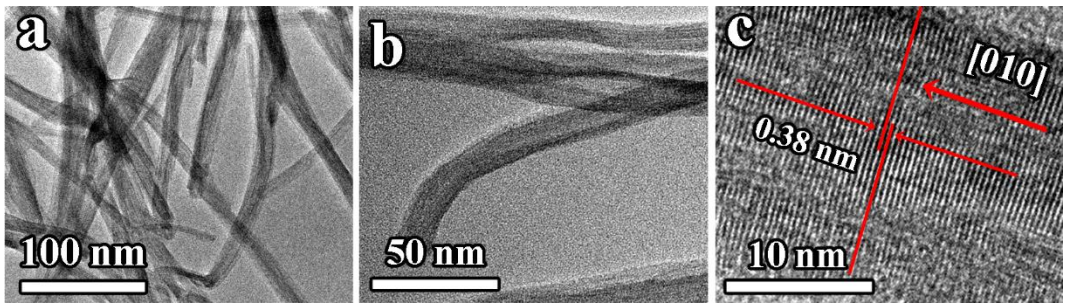

Fig. 3 Low and high magnification TEM images of (a–c) the nanowire $WO_{2.72}$/carbon cloth.

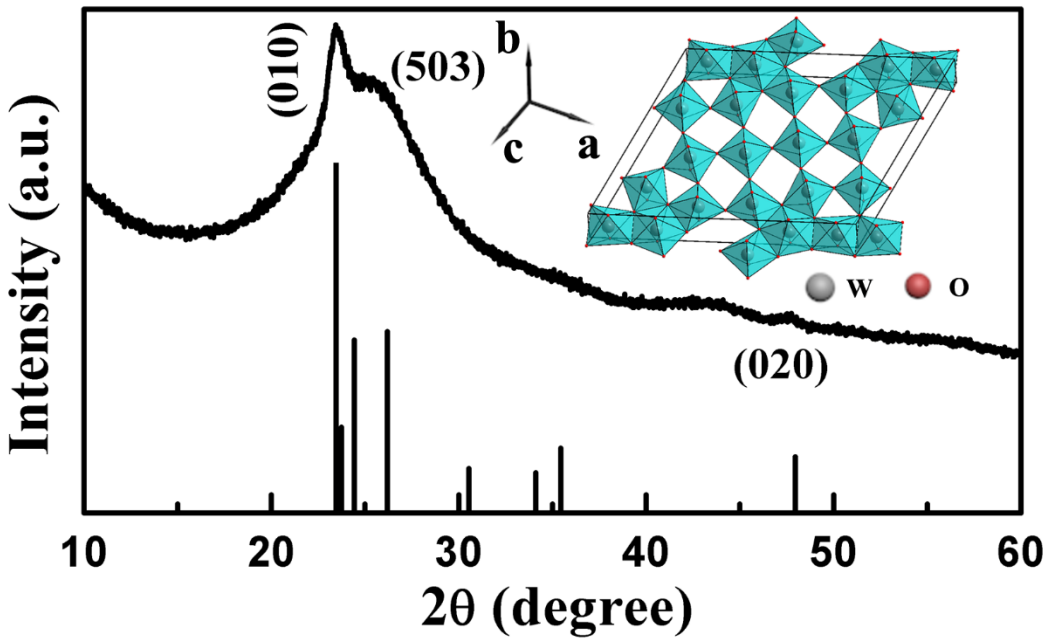

Fig. 4 XRD pattern of nanowire $WO_{2.72}$/carbon cloth (JCPDS file #65-1291), inset: an illustration of the crystal structure of the close-packed (010) planes.

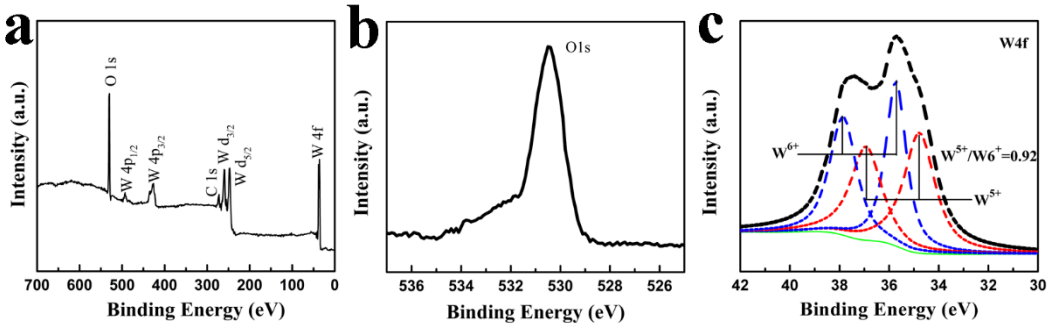

Fig. 5 XPS spectra of nanowire $WO_{2.72}$/carbon cloth, (a) the survey spectrum, (b) O1s and (c) W4f.

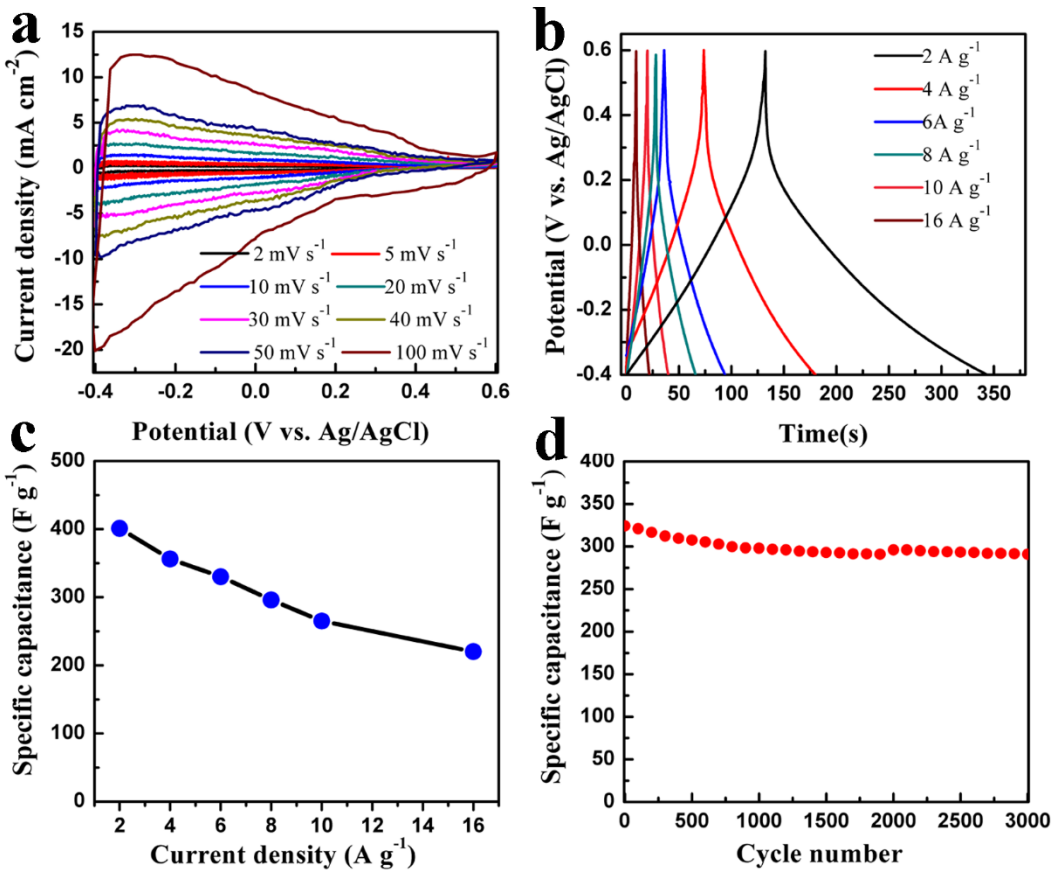

Fig. 6 (a) CV curves, (b) GCD curves, (c) Cs versus current densities and (d) cycle life at current density of 6 A g^{-1} of nanowire $WO_{2.72}$/carbon cloth in 5 M LiCl aqueous solution.

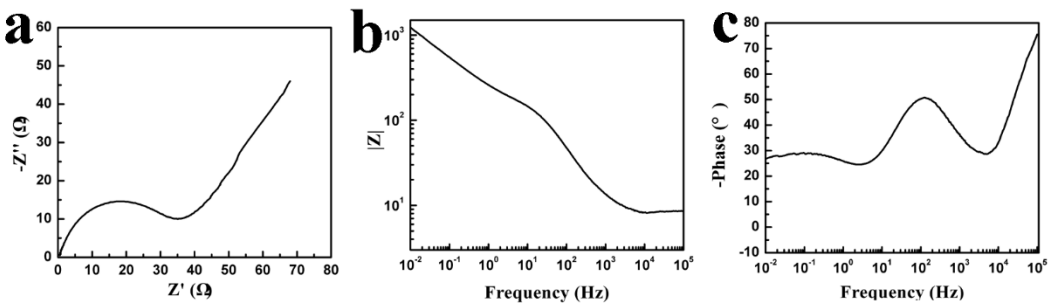

Fig. 7 (a) Nyquist plot, (b) Bode plot of f–|Z| (a) and (c) Bode phase angle plot.

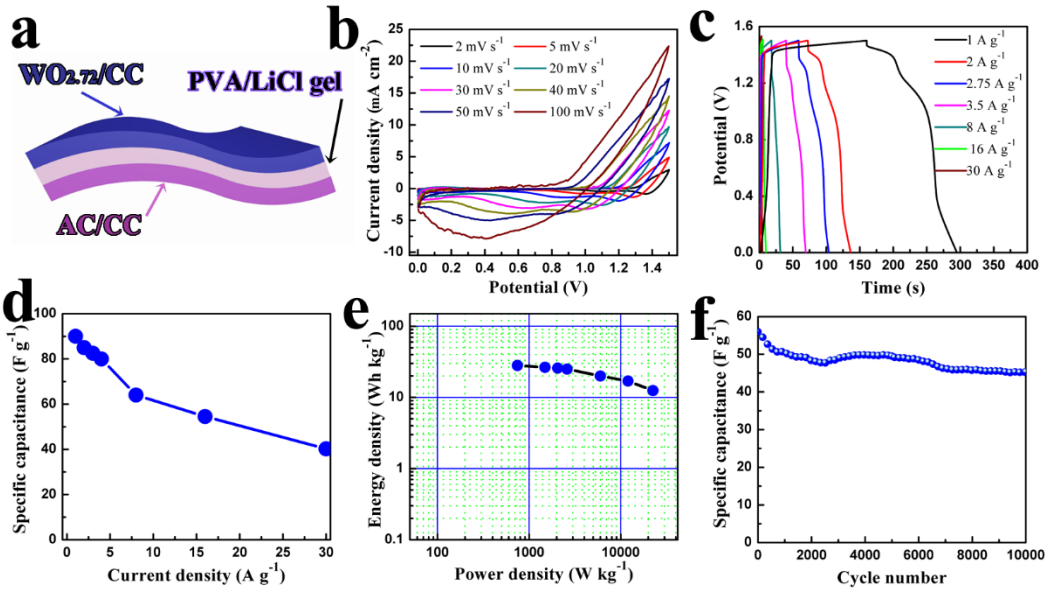

Fig. 8 (a) schematic illustration of the FASCs device, (b) CV curves of FASCs collected at different scanning rates, (c) GCD curves of the FASCs, (d) Cs versus current densities, (e) Ragone plot and (f) Cycling stability of the FASCs.